PCCP

PAPER

View Article Online
View Journal | View Issue

Cite this: *Phys. Chem. Chem. Phys.*, 2014, **16**, 728

Influence of La-doping on phase transformation and photocatalytic properties of $ZnTiO_3$ nanoparticles synthesized *via* modified sol–gel method†

T. Surendar, Santosh Kumar and Vishnu Shanker*

Received 11th September 2013,
Accepted 18th October 2013

DOI: 10.1039/c3cp53855a

www.rsc.org/pccp

Non-doped and La-doped $ZnTiO_3$ nanoparticles were successfully synthesized *via* a modified sol–gel method. The synthesized nanoparticles were structurally characterized by PXRD, UV-vis DRS, FT-IR, SEM-EDS, TEM, Raman and photoluminescence spectroscopy. The results show that doping of La into the framework of $ZnTiO_3$ has a strong influence on the physico-chemical properties of the synthesized nanoparticles. XRD results clearly show that the non-doped $ZnTiO_3$ exhibits a hexagonal phase at 800 °C, whereas the La-doped $ZnTiO_3$ exhibits a cubic phase under similar experimental conditions. In spite of the fact that it has a large ionic radius, the La is efficiently involved in the evolution process by blocking the crystal growth and the cubic to hexagonal transformation in $ZnTiO_3$. Interestingly the absorption edge of the La-doped $ZnTiO_3$ nanoparticles shifted from the UV region to the visible region. The photocatalytic activity of the La-doped $ZnTiO_3$ nanoparticles was evaluated for the degradation of Rhodamine B under sunlight irradiation. The optimum photocatalytic activity was obtained for 2 atom% La-doped $ZnTiO_3$, which is much higher than that of the non-doped $ZnTiO_3$ as well as commercial N-TiO_2. A possible mechanism for the degradation of Rhodamine B over La-doped $ZnTiO_3$ was also discussed by trapping experiments. More importantly, the reusability of these nanoparticles is high. Hence La-doped $ZnTiO_3$ nanoparticles can be used as efficient photocatalysts for environmental applications.

Introduction

In recent years, nanostructured materials have attracted considerable attention for photocatalysis due to their unique physical and chemical properties compared to their bulk counterparts.[1–3] Photocatalysis is an important chemical process that underpins the development of critical renewable energy sources and environmental technologies such as photocatalytic water purification, hydrogen production from water splitting and high-efficiency solar cells. It is a catalytic process occurring on the surface of semiconductor materials under the irradiation of photons.[4–7] To date, most of the investigations on photocatalysis have focused on enhancing the photocatalytic activity of semiconductor materials such as titania (TiO_2).[8,9] However, the design and development of visible light driven nanostructured photocatalysts is today's research interest. Recently, perovskite zinc titanate ($ZnTiO_3$) has been investigated due to its wide range of applications in microwave dielectrics, sorbents for the desulfurization of hot coal gases, paint pigments, gas sensors and more preferably for low temperature co-fired ceramics.[10–17] In addition, $ZnTiO_3$ is one of the important photocatalysts and has been widely used for degradation of organic compounds.[18]

Fundamental studies concerning the phase diagram and the characterization of the ZnO–TiO_2 system have been published by Dulin and Rase.[19,20] This system is still attracting the attention of researchers as ZnO and TiO_2 are wide band gap semiconductors with several favorable properties and extensive applications using either the single material or ZnO–TiO_2 composites. The simultaneous synthesis of a ZnO–TiO_2 composite usually results in the formation of three known compounds from the ZnO–TiO_2 system: $ZnTiO_3$ (cubic, hexagonal), Zn_2TiO_4 (cubic, tetragonal) and $Zn_2Ti_3O_8$ (cubic).[19–21] $Zn_2Ti_3O_8$ is the metastable, low-temperature form of $ZnTiO_3$.[22] However, pure $ZnTiO_3$ is not easily obtained because it transforms to Zn_2TiO_4 and rutile upon sintering.[19,21] There are several reports on synthesizing $ZnTiO_3$ nanoparticles such as by a solid state reaction[19] and by the sol–gel method.[22,23] The sol–gel method has been successfully applied over the past two decades in the synthesis of ceramics, fibers, glasses, and thin films. It has shown considerable advantages over conventional solid state reactions.

Department of Chemistry, National Institute of Technology, Warangal-506 004, A.P., India. E-mail: vishnu@nitw.ac.in; Fax: +91-870-2459547; Tel: +91-870-2462675

† Electronic supplementary information (ESI) available. See DOI: 10.1039/c3cp53855a

These advantages include excellent compositional control, homogeneity at the molecular level due to the mixing of liquid precursors, and lower crystallization temperatures.[24–27]

On the other hand, the perovskite (ABO_3) structure provides the flexibility to vary the composition of the A and B sites and to incorporate a combination of cations at the A and B sites to form substituted perovskites. In an ABO_3 perovskite, varying the stoichiometry or doping with a cation of a different valence state can, in principle, change the electronic properties.[28] Therefore, doping is a powerful strategy to modify the basic structure and hence the electronic and catalytic properties of the substituted perovskites. In this paper, we report the synthesis of La-doped $ZnTiO_3$ nanoparticles by a modified sol–gel method. The synthesized nanoparticles were structurally characterized by various analytical techniques. The influence of La-doping on physicochemical properties like crystal growth, phase transformation and optical properties of the synthesized nanoparticles were investigated. The photocatalytic activity was also evaluated towards the degradation of Rhodamine B (RhB) under sunlight irradiation.

Experimental details

Materials

Titanium isopropoxide (Sigma-Aldrich, 99.9% trace metals basis), Rhodamine B (Sigma-Aldrich, 95.0% dye content), zinc acetate dihydrate (SRL, 99.5%), lanthanum nitrate hexahydrate (SRL, 99.0%), terephthalic acid (Merck, AR), *tert*-butyl alcohol (Merck, AR) ethylene glycol (SRL, 99.0%), and ethanol (SDFCL, 99.9%) were used as received. All other reagents used in this work were of analytically pure grade and used without further purification.

Method

Non-doped and La-doped $ZnTiO_3$ nanoparticles were synthesized by a modified sol–gel method. In brief the experimental procedure was as follows. The titanium isopropoxide was dissolved in absolute ethanol with a volume ratio of 1 : 4 under vigorous stirring for about 30 min at room temperature. To this solution, a calculated amount of conc. HCl and doubly distilled water was added drop wise as a catalyst to increase the rate of reaction, and for the hydrolysis reaction, respectively. The resulting solution was kept under stirring at room temperature to form a TiO_2 sol. To this TiO_2 sol, the required amount of zinc acetate dihydrate (Zn : Ti = 1 : 1) dissolved in ethylene glycol was added slowly under stirring. However, for the preparation of the La-doped zinc titanate $(Zn_{1-x}La_x)TiO_3$ (x = 0.01, 0.02, 0.03, 0.04 and 0.05) nanoparticles, the stoichiometric amount of lanthanum nitrate hexahydrate along with zinc acetate dihydrate were dissolved in ethylene glycol. The above reaction mixture was heated at 120 °C for 5 h to form a white colored gel. The formed gel was charred at 350 °C with a slow heating rate and ground to obtain a fine powder. Subsequently, the synthesized product was calcined at different temperatures for 3 h. The obtained non-doped $ZnTiO_3$ powder was denoted as ZT and the obtained 1–5 atom% La doped $ZnTiO_3$ samples were denoted as ZLT-1, ZLT-2, ZLT-3, ZLT-4 and ZLT-5 respectively.

Characterization

Powder X-ray diffraction studies (PXRD) were carried out on a Bruker AXS D8 Advance diffractometer using Ni filtered Cu Kα (λ = 1.5406 Å) radiation in the scan range of 2θ between 20° and 80°. UV-vis diffuse reflectance spectra (UV-DRS) were recorded on a Lambda 20 instrument (UV-vis NIR spectrophotometer), equipped with an integrating sphere, and $BaSO_4$ was used as a reference. FT-IR spectra were recorded in transmission mode from 4000 to 400 cm^{-1} on a PerkinElmer Spectrum 100 FT-IR Spectrophotometer using KBr discs. Raman studies were carried out on a PerkinElmer RamanStation 400 spectrometer with a 785 nm laser as the excitation source. The surface morphology and composition of the samples were investigated by scanning electron microscopy (SEM; JEOL Model JSM-6390LV) and energy dispersive spectroscopy (EDS; JEOL Model JED-2300). The nanostructures were observed using a FEI Tecnai G2 Series transmission electron microscope (TEM) operating at 200 kV. The surface area measurements were recorded by using Quanta chrome NOVA 1200e and the surface area of the catalysts were estimated using a BET method. UV-visible absorption spectra (UV-vis) were recorded on a THERMO Scientific Evolution 600 UV-vis NIR spectrophotometer. The photoluminescence (PL) spectra of the photocatalysts were recorded on a TSC Solutions F96pro fluorescence spectrophotometer at an excitation wavelength of 365 nm.

Photocatalytic activity

The photocatalytic activity of the synthesized samples (0.1 g) was examined by monitoring the degradation of RhB in an aqueous solution (250 mL, 5 mg L^{-1}) under sunlight irradiation. Photocatalytic experiments of all the samples were carried out under similar conditions on sunny days between 11 a.m. and 4 p.m. in the month of April 2013 at NIT Warangal, as the fluctuations in the sunlight intensity is minimal during this month. Prior to irradiation, the solution was first stirred in the dark for 30 min to reach the adsorption equilibrium. During the sunlight irradiation, the reaction solution was periodically withdrawn, centrifuged to separate the photocatalyst, and used for the absorbance measurements by UV-vis spectrophotometry. A blank test was also carried out for the RhB aqueous solution without the photocatalyst under sunlight irradiation *i.e.*, the photolysis of RhB was carried out to evaluate the efficiency of the photocatalyst.

Analysis of reactive species

The reactive species analysis was similar to the photodegradation experimental process. Various scavengers were introduced to the RhB solution prior to the addition of the photocatalyst. Furthermore, photoluminescence (PL) spectra with terephthalic acid (TA) as a probe molecule were used to observe the formation of $^{\bullet}OH$ on the surface of the photocatalyst under sunlight irradiation. A brief experimental procedure is as follows. 0.1 g of a 2 atom% La-doped $ZnTiO_3$ (ZLT-2) sample was dispersed in 100 mL of a 5×10^{-4} mol L^{-1} TA aqueous solution with a 2×10^{-3} mol L^{-1} concentration of NaOH at room temperature. The resulting solution was magnetically stirred and the

suspension was exposed to sunlight. The suspension was collected at 5 min intervals and centrifuged to measure the maximum PL intensity using fluorescence spectrophotometry with an excitation wavelength of 365 nm.

Results and discussion

Fig. 1 shows the XRD patterns of non-doped and La-doped $ZnTiO_3$ samples calcined at 800 °C for 3 h. The patterns show that the samples are well crystallized. The diffraction peaks of the non-doped $ZnTiO_3$ are in good agreement with the hexagonal crystal phase of $ZnTiO_3$ (JCPDS No. 26-1500) whereas, the diffraction peaks of the La-doped $ZnTiO_3$ samples are in good agreement with the cubic crystal phase of $ZnTiO_3$ (JCPDS No. 39-0190). However, no peaks corresponding to the TiO_2, ZnO or zinc titanates of other stoichiometry were observed, which indicates that a proper Zn/Ti ratio is maintained in the synthesis of the non-doped and La-doped $ZnTiO_3$ nanoparticles. A significant diffraction peak broadening after the La doping indicates a decreasing crystallinity due to the incorporation of La into the $ZnTiO_3$ crystal structure. The average crystallite size of the non-doped and La-doped $ZnTiO_3$ nanoparticles was also calculated using the Scherrer equation. It is observed that the average crystallite size of ZLT-2 (15 nm) is much lower than the non-doped $ZnTiO_3$ (47 nm). This is because many crystal defects may be formed when the dopant ions occupy regular lattice sites of $ZnTiO_3$. As a result, the formed defects inhibit the growth of the crystal, and therefore decreases the crystal size. However, the average crystallite size was found to be decreased with an increase in La content up to 2 atom% and slightly increased with a further increase in La content as shown in Fig. S1 (ESI†).

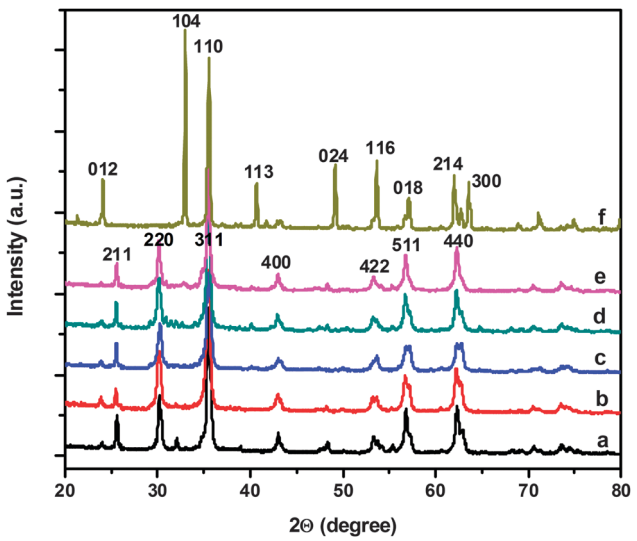

Fig. 1 XRD patterns of the synthesized non-doped and La-doped $ZnTiO_3$ nanoparticles calcined at 800 °C for 3 h: (a) ZLT-1 (b) ZLT-2 (c) ZLT-3 (d) ZLT-4 (e) ZLT-5 and (f) ZT.

Effect of La-doping on phase transformation

The XRD patterns of the non-doped $ZnTiO_3$ and La-doped $ZnTiO_3$ (ZLT-2) nanoparticles calcined at different temperatures for 3 h are shown in Fig. 2a and b respectively, to observe the temperature effect on the phase transformation. As can be seen from Fig. 2a the non-doped $ZnTiO_3$ sample calcined at 500 °C showed the cubic $ZnTiO_3$ peaks with poor crystallinity. When the calcination temperature increased to 600 °C the cubic phase of $ZnTiO_3$ was retained, but the peak intensity was greatly increased because an increase in the calcination temperature can enhance the atomic mobility, which causes grain growth and better crystallinity. Furthermore, a phase change from cubic to hexagonal was observed with an increase in the calcination temperature from 600 to 700 °C. The pure hexagonal phase of $ZnTiO_3$ was obtained at a calcination temperature of 800 °C. Fig. 2b shows the cubic phase of La-doped $ZnTiO_3$ at different calcination temperatures. However, the peak intensity was greatly increased with an increase in the calcination temperature, which is similar to non-doped $ZnTiO_3$, but interestingly no phase change was observed in the La-doped $ZnTiO_3$ nanoparticles. This implies that the incorporated La was efficiently involved in the evolution process by blocking the crystal growth and the cubic to hexagonal transformation in $ZnTiO_3$. A similar phenomenon was

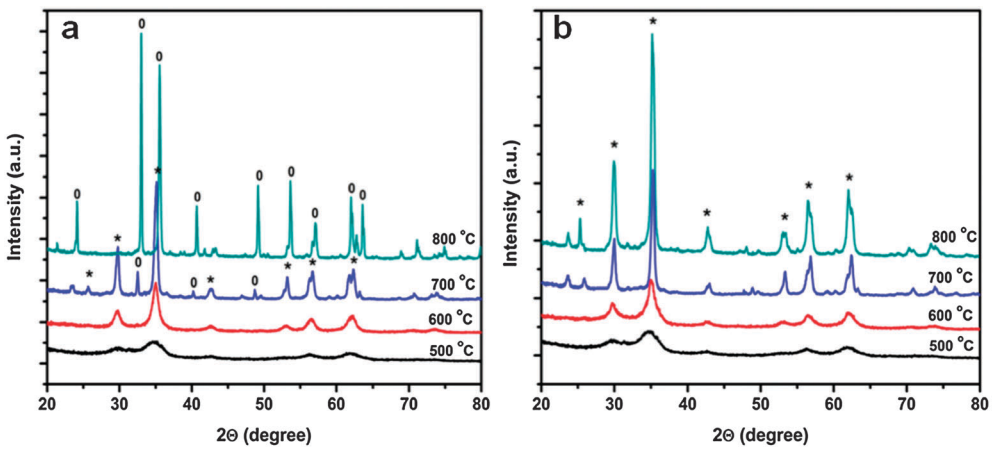

Fig. 2 XRD patterns of the synthesized non-doped and La-doped $ZnTiO_3$ nanoparticles calcined at various temperatures for 3 h: (a) ZT and (b) ZLT-2 (* – cubic and 0 – hexagonal phases).

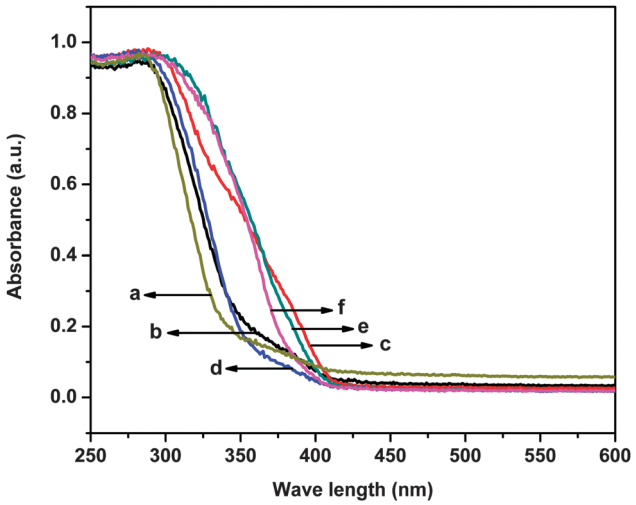

Fig. 3 UV-vis diffuse reflectance spectra of the synthesized non-doped and La-doped $ZnTiO_3$ nanoparticles: (a) ZT (b) ZLT-1 (c) ZLT-2 (d) ZLT-3 (e) ZLT-4 and (f) ZLT-5.

also observed in Eu^{3+}-doped $ZnTiO_3$ by Mrazek *et al.*[29] It is also observed that the diffraction intensity of the La-doped $ZnTiO_3$ samples at all calcination temperatures is very low compared to the non-doped $ZnTiO_3$ as shown in Fig. S2 (ESI†).

Fig. 3 shows the UV-vis diffuse reflectance spectra of the non-doped and La-doped $ZnTiO_3$ nanoparticles. The absorption in the visible region of the La-doped $ZnTiO_3$ is due to the electron donor levels formed by the La impurity in the lattice structure of $ZnTiO_3$. Because La doping introduces n-type carriers in the $ZnTiO_3$ system, the Fermi level shifts into the conduction band. A similar phenomenon was also reported in Cr-doped $SrTiO_3$ by Wang *et al.*[30] and in La-doped Sr_2TiO_4 by Wang *et al.*[31] Owing to the lower energy separation between the new energy levels and the valance or conduction band, visible light becomes energetic enough to accelerate the electron transitions. Therefore, the La-doped $ZnTiO_3$ probably generates more free charge carriers to induce surface chemical reactions than that of the pure $ZnTiO_3$ under sunlight irradiation, because the sunlight is composed of about 50% visible light. The band gap energy is obtained by plotting $(\alpha h\nu)^2$ *vs.* $h\nu$ where α is the absorption coefficient and $h\nu$ is photon energy. Extrapolation of the linear portion at $(\alpha h\nu)^2 = 0$ gives the band gap energy for a particular sample. The estimated band gap energy from the intercept of the tangents to the plots are 3.54, 3.37, 2.92, 3.35, 3.01 and 3.12 eV for the samples ZT, ZLT-1, ZLT-2, ZLT-3, ZLT-4 and ZLT-5 respectively. Thus, the minimum energy required to excite an electron from the valence band to the conduction band is considerably lower in the La-doped $ZnTiO_3$ than that of the non-doped $ZnTiO_3$. This concludes that the La-doped $ZnTiO_3$ has a larger redox potential for the photocatalytic decomposition of organic contaminants under sun light irradiation.

Fig. 4A shows the FT-IR spectrum of the synthesized non-doped and La-doped $ZnTiO_3$ nanoparticles at 800 °C for 3 h. The bands above 400 cm^{-1} are due to Ti–O stretching vibrations and those below 400 cm^{-1} are due to Ti–O bending vibrations.[32] It is also seen that these main characteristic peaks of $ZnTiO_3$ are shifted to a lower wavenumber region in the La-doped $ZnTiO_3$ nanoparticles as shown in Fig. S3 (ESI†). The red shift of these bands indicates a change in the bond strengths of Zn–Ti–O, suggesting the successful doping of La into the $ZnTiO_3$ crystal structure. Furthermore, the intensity of the peaks was greatly suppressed with an increase in the La content in the La-doped $ZnTiO_3$ nanoparticles. This implies that the incorporated La was efficiently involved in the evolution process by blocking the crystal growth in $ZnTiO_3$. However, the broad bands observed in all samples at around 3466 cm^{-1} and 1658 cm^{-1} correspond to the stretching and bending vibrations of O–H in the adsorbed H_2O molecules respectively. The spectral data of hexagonal and cubic phases of the non-doped and La-doped $ZnTiO_3$ are in good agreement with the results reported elsewhere by Yamaguchi *et al.*[22]

Raman spectra were recorded with a 785 nm laser as the excitation source to further investigate the phase transformation. Fig. 4B shows the Raman spectra of the synthesized non-doped and La-doped $ZnTiO_3$ nanoparticles calcined at 800 °C for 3 h. It can be clearly seen that the non-doped and La-doped

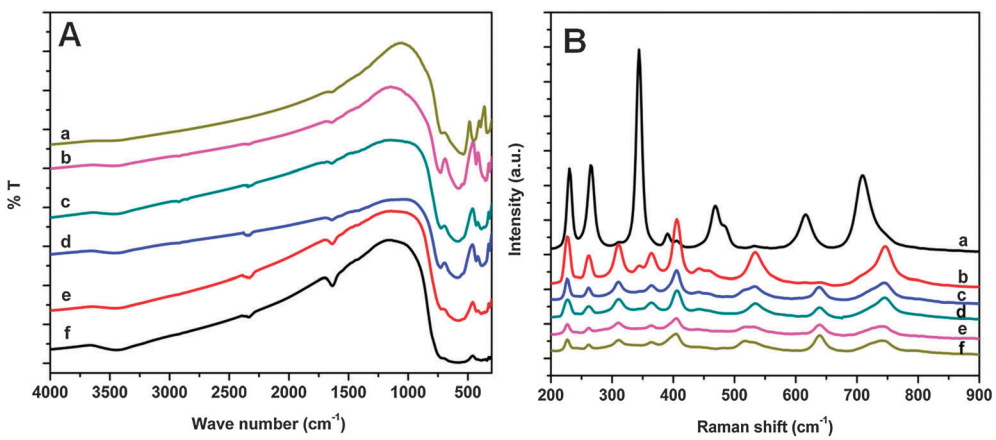

Fig. 4 FT-IR spectra (A) and Raman spectra (B) of the synthesized non-doped and La-doped $ZnTiO_3$ nanoparticles: (a) ZT (b) ZLT-1 (c) ZLT-2 (d) ZLT-3 (e) ZLT-4 and (f) ZLT-5.

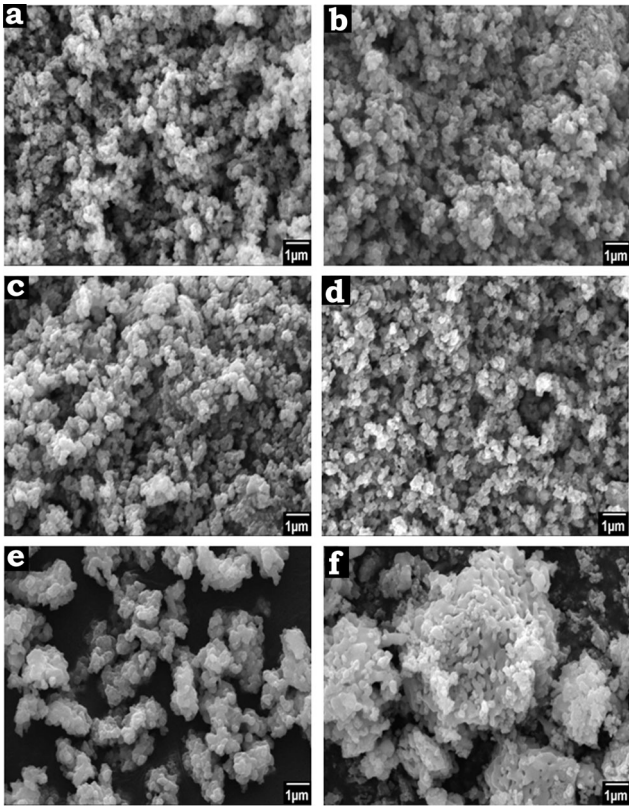

Fig. 5 SEM images of the synthesized non-doped and La-doped $ZnTiO_3$ nanoparticles: (a) ZT (b) ZLT-1 (c) ZLT-2 (d) ZLT-3 (e) ZLT-4 and (f) ZLT-5.

$ZnTiO_3$ nanoparticles show different patterns. For the non-doped $ZnTiO_3$, the peaks observed at around 261, 342, 528 and 713 cm^{-1} are attributed to the vibration modes of ν_4(LO), ν_2(LO, TO), ν_1(TO) and ν_1(LO), respectively, which are the characteristic peaks of hexagonal $ZnTiO_3$. The Raman peaks appearing around 520 and 234 cm^{-1} are attributed to the vibration modes of ν_1(TO) and ν_4(LO) respectively, which are characteristic peaks of the cubic phase present in the La-doped $ZnTiO_3$.[33,34] It has been observed that with an increasing La content, most of the peaks broaden and shift towards the lower frequencies. The above results are in good agreement with the XRD analysis as discussed above.

Fig. 5 shows the SEM images of the non-doped and La-doped $ZnTiO_3$ nanoparticles calcined at 800 °C for 3 h. As can be observed in Fig. 5(a–f), the non-doped and La doped $ZnTiO_3$ nanoparticles possess hemi-spherical morphology with fine particles and uniform size distribution. Moreover, the $ZnTiO_3$ nanoparticles were highly agglomerated with an increase in the La content in the La-doped $ZnTiO_3$ thereby decreasing the photocatalytic activity by blocking the active sites on the surface of the $ZnTiO_3$ nanoparticles. In addition, X-ray energy dispersive spectroscopy (EDS) was used to determine the chemical composition of the synthesized samples (Fig. S4, ESI†). The results reveal that the molar ratio of Zn to Ti is about 1 : 1 within the instrumental accuracy for the non-doped $ZnTiO_3$. The La doping content in the La-doped $ZnTiO_3$ nanoparticles identified by the EDS results is similar to the loaded content as listed in Table 1.

Table 1 Physical and textural properties of non-doped and La-doped $ZnTiO_3$ nanoparticles

Sample	La loading (atom%)	Actual La loading (from EDS) (atom%)	Crystallite size (nm)	Energy gap (eV)
ZT	0	0	47	3.54
ZLT-1	1	1.07	25	3.37
ZLT-2	2	1.98	15	2.92
ZLT-3	3	2.87	18	3.35
ZLT-4	4	3.99	22	3.01
ZLT-5	5	4.65	24	3.12

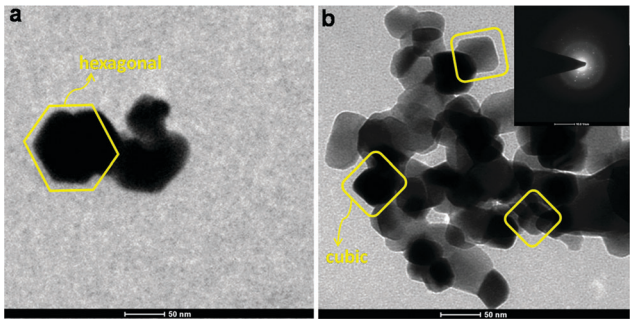

Fig. 6 TEM images of the synthesized (a) ZT and (b) ZLT-2 sample and corresponding selected area electron diffraction (SAED) pattern (inset).

Fig. 6 shows the TEM images of the non-doped $ZnTiO_3$ and La-doped $ZnTiO_3$ (ZLT-2) nanoparticles. The TEM results support the hexagonal and cubic structure of the non-doped $ZnTiO_3$ (Fig. 6a) and La-doped $ZnTiO_3$ nanoparticles (Fig. 6b), respectively. The particle sizes range around 40–50 nm for the non-doped $ZnTiO_3$ and 20–30 nm for the La-doped $ZnTiO_3$, which are in good agreement with the corresponding crystallite size calculated using the Scherrer equation. Furthermore, a selected area electron diffraction (SAED) pattern shown in the inset of Fig. 6b also resembles closely the cubic perovskite $ZnTiO_3$ structure.

The specific surface area of the non-doped $ZnTiO_3$ (ZT) and La-doped $ZnTiO_3$ (ZLT-2) nanoparticles was investigated by nitrogen adsorption isotherm analysis. The specific surface area of the ZT and ZLT-2 samples was found to be 10.77 $m^2\ g^{-1}$ and 15.25 $m^2\ g^{-1}$ respectively. The relatively large specific surface area of the La-doped $ZnTiO_3$ nanoparticles is useful for the better adsorption of organic compounds and also provides a greater number of reactive sites for the photocatalytic process, thereby enhancing the photocatalytic activity.

Photocatalytic performance

The photocatalytic activity of the synthesized samples was evaluated for the degradation of RhB under sunlight irradiation, as shown in Fig. 7A. The photolysis of RhB under the same experimental conditions (in the absence of a catalyst) indicates that RhB is stable under sunlight irradiation. The synthesized La-doped $ZnTiO_3$ nanoparticles exhibit a much higher photocatalytic activity than that of the non-doped $ZnTiO_3$ and commercial N-TiO_2. The optimum photocatalytic activity was obtained for a 2 atom% La-doped $ZnTiO_3$. However, the photocatalytic activity of the La-doped $ZnTiO_3$ increased at first by doping

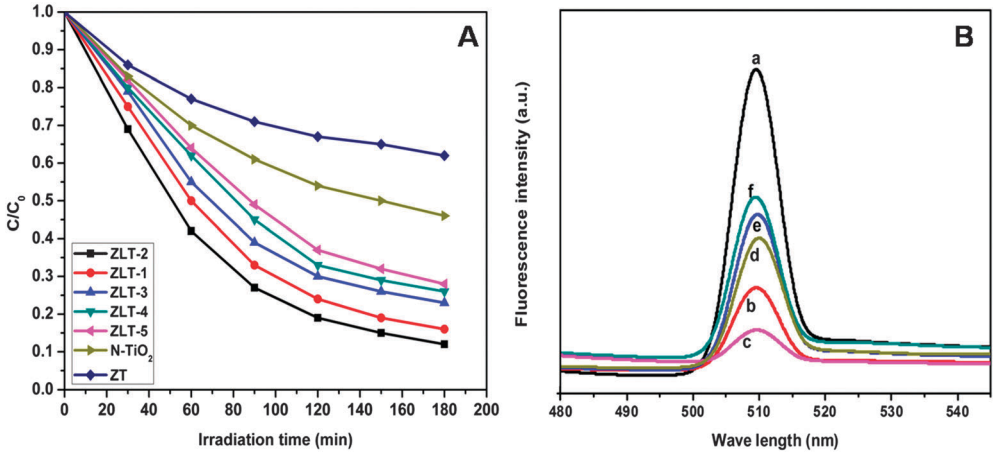

Fig. 7 (A) Comparison of photocatalytic activities for the degradation of RhB in aqueous solution under sunlight irradiation over non-doped and La-doped $ZnTiO_3$ nanoparticles; (B) room temperature photoluminescence (PL) spectra of the synthesized non-doped and La-doped $ZnTiO_3$ nanoparticles excited at 365 nm: (a) ZT (b) ZLT-1 (c) ZLT-2 (d) ZLT-3 (e) ZLT-4 and (f) ZLT-5.

with 2 atom% La, and then decreased with an increase in La content. The decrease in the photocatalytic activity by doping with excess amounts of La^{3+} may be due to following reasons: (1) the increase in the amount of oxygen vacancies, which become the recombination centers for the photoinduced electrons and holes[35] and (2) the high agglomeration in the nanoparticles which can block the active sites on the surface of the $ZnTiO_3$ nanoparticles. Therefore, the order of photocatalytic activity of the synthesized samples for the degradation of RhB under sunlight irradiation was summarized as follows; ZLT-2 > ZLT-1 > ZLT-3 > ZLT-4 > ZLT-5 > ZT.

Photoluminescence

The enhanced photocatalytic activity of the La-doped $ZnTiO_3$ can be explained by photoluminescence (PL) spectra, which explain the migration, transfer and recombination processes of the photoinduced electron–hole pairs in semiconductor materials.[36] Fig. 7B shows the PL spectra of the synthesized non-doped and La-doped $ZnTiO_3$ nanoparticles recorded at room temperature with an excitation wavelength of 365 nm. It can be seen that the non-doped $ZnTiO_3$ sample has a strong peak around 510 nm in the PL spectrum. Interestingly, the PL intensity has been greatly decreased due to the hindered recombination rate of the photoinduced electron–hole pairs in the La-doped $ZnTiO_3$ nanoparticles.

Possible mechanism for enhanced photocatalytic performance

According to the theoretical band structure, the $ZnTiO_3$ has a large band gap (3.8 eV) with a valance edge potential of +3.0 eV which is predominated by O 2p states and a conduction edge potential of −0.8 eV determined by Ti 3d states.[37–39] The photoinduced electron in the conduction band of $ZnTiO_3$ can produce $O_2^{\bullet-}$ from adsorbed O_2 because the valance edge potential of $ZnTiO_3$ is more negative than ($E_{(O_2/O_2^{\bullet-})}$ = −0.3 eV *vs.* NHE).[36,40,41] Meanwhile the trapped holes in the valance band of $ZnTiO_3$ can oxidize the H_2O to yield $^{\bullet}OH$ because the conduction edge potential of $ZnTiO_3$ is more positive than ($E_{(^{\bullet}OH/H_2O^{\bullet})}$ = +2.68 eV *vs.* NHE).

Detection of reactive species

To examine the role of these reactive species in the La-doped $ZnTiO_3$ system, the effects of some radical scavengers and N_2 purging on the photodegradation of RhB were investigated. It can be seen from Fig. 8a, on the addition of *tert*-butyl alcohol (*t*-BuOH) which acts as an $^{\bullet}OH$ scavenger, that the degradation rate was drastically inhibited for the photocatalytic degradation of RhB compared with no scavenger at the same conditions. A significant change was observed in the degradation rate with the addition of ammonium oxalate (AO) acting as a hole scavenger. Meanwhile, a small change in the degradation of RhB was observed when N_2 purging was conducted which acts as an $O_2^{\bullet-}$ scavenger, suggesting that the hole and $^{\bullet}OH$ are major reactive species in La-doped $ZnTiO_3$ photocatalysts.

Hydroxyl radical generation

To probe the generation of $^{\bullet}OH$ in the sunlight irradiated suspension of the ZLT-2 sample, terephthalic acid (TA) was added as a reagent, which readily reacts with $^{\bullet}OH$ to produce the highly fluorescent product 2-hydroxyterephthalic acid. A maximum intensity peak in the PL spectra was observed at around 425 nm with an excitation wavelength of 365 nm as shown in Fig. 8b. It is also observed from Fig. 8b that the PL intensity increases gradually with an increasing irradiation time, which demonstrates that $^{\bullet}OH$ is indeed generated on the sunlight irradiated surface of the La-doped $ZnTiO_3$ showing a markedly enhanced production of 2-hydroxyterephthalic acid. The results confirm the formation of $^{\bullet}OH$ on the surface of the photocatalyst, which leads to the enhanced photocatalytic activity for the degradation of RhB under sunlight irradiation as shown in Fig. 9a.

Reusability

The reusability of a photocatalyst is one of the important factors for its practical application. However, the La-doped $ZnTiO_3$ nanoparticles can be easily reused by a simple filtration

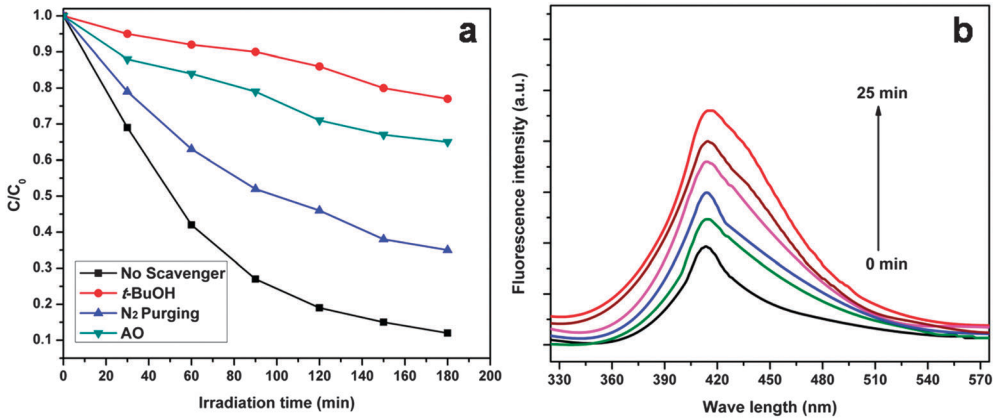

Fig. 8 (a) Effect of different scavengers on the degradation of RhB in the presence of ZLT-2 catalyst under sunlight irradiation, (b) •OH trapping PL spectra of ZLT-2 with TA solution under sunlight irradiation.

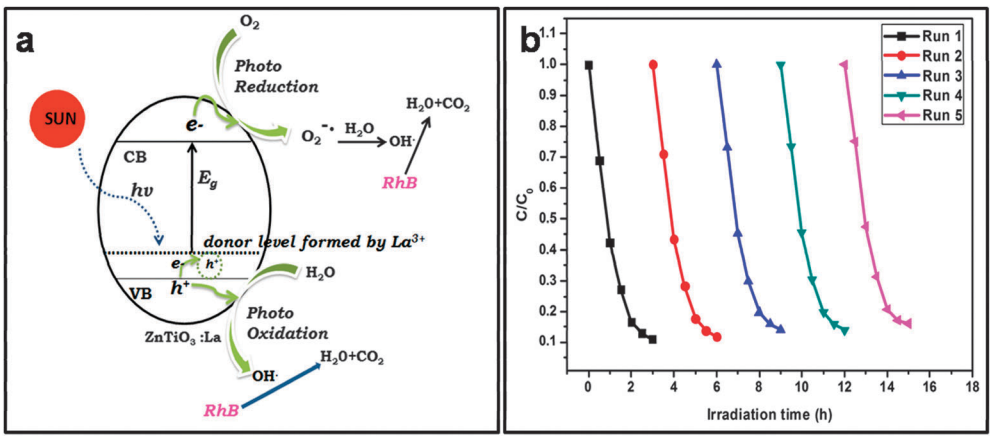

Fig. 9 (a) Schematic illustration of the high photocatalytic activity of La-doped $ZnTiO_3$ nanoparticles for the degradation of RhB in aqueous solution under sunlight irradiation; (b) reusability of the ZLT-2 photocatalyst in five successive experimental runs for the photocatalytic degradation of RhB in aqueous solution under sunlight irradiation.

or by low-speed centrifugation and thus avoids a secondary pollution. To study the reusability of the La-doped $ZnTiO_3$ nanoparticles, five successive photocatalytic runs were carried out by adding recycled La-doped $ZnTiO_3$ to fresh RhB solutions with no change in the overall concentration of the catalyst under sunlight irradiation. The photocatalytic activity of the ZLT-2 sample is retained over 90% of its original activity after five successive experimental runs under sunlight irradiation as shown in Fig. 9b. Therefore, the La-doped $ZnTiO_3$ nanoparticles can be used as high-performance visible light photocatalysts with potential applications in environmental protection.

Conclusion

Non-doped and La-doped $ZnTiO_3$ nanoparticles have been successfully synthesized by a modified sol–gel method. The results indicated that the non-doped $ZnTiO_3$ showed a hexagonal phase at 800 °C for 3 h whereas the La-doped $ZnTiO_3$ showed a cubic phase. The crystal structure, particle size and band structure of $ZnTiO_3$ were significantly affected due to La-doping. Interestingly, the La-doped $ZnTiO_3$ nanoparticles show a much higher photocatalytic activity compared to the non-doped $ZnTiO_3$ as well as commercial N-TiO_2. The highest photocatalytic activity is observed for 2 atom% La-doped $ZnTiO_3$ nanoparticles. The improved photocatalytic performance of the La-doped $ZnTiO_3$ nanoparticles under sunlight irradiation is due to a synergistic effect within the crystal structure. Significant decreases in particle size lead to an increase in the surface area and subsequently provide more reactive sites on the surface of the photocatalyst and absorption in the visible region. Interestingly, the synthesized La-doped $ZnTiO_3$ photocatalyst possesses high reusability. Therefore, the synthesized photocatalysts will be of great value to the efficient utilization of solar energy and can be used for environmental remediation.

Acknowledgements

The authors thank the Department of Science and Technology, Government of India for financial support (SR/FT/CS-096/2009).

References

1 K. Sivula, F. Le Formal and M. Gratzel, *ChemSusChem*, 2011, **4**, 432–449.
2 N. S. Lewis and D. G. Nocera, *Proc. Natl. Acad. Sci. U. S. A.*, 2006, **103**, 15729–15735.
3 D. Ginley, M. A. Green and R. Collins, *MRS Bull.*, 2008, **33**, 355–372.
4 A. Fujishima and K. Honda, *Nature*, 1972, **238**, 37–38.
5 P. V. Kamat, *Chem. Rev.*, 1993, **93**, 267–300.
6 A. Hagfeldt and M. Gratzel, *Chem. Rev.*, 1995, **95**, 49–68.
7 T. L. Thompson and J. T. Yates, *Chem. Rev.*, 2006, **106**, 4428–4458.
8 Y. M. Wang, Y. Huang, W. K. Ho, L. Z. Zhang, Z. G. Zou and S. C. Lee, *J. Hazard. Mater.*, 2009, **169**, 77–87.
9 Y. Xie, X. Zhao, Y. Li, Q. Zhao, X. Zhou and Q. Yuan, *J. Solid State Chem.*, 2008, **181**, 1936–1942.
10 H. T. Kim, J. D. Byun and Y. Kim, *Mater. Res. Bull.*, 1998, **33**, 975–986.
11 Z. X. Chen, J. Van der Berg, W. Koot, R. Van der Berg, J. Van Mechelen and A. Derking, *J. Am. Ceram. Soc.*, 1995, **78**, 2993–3001.
12 H. Obayashi, Y. Sakurai and T. Gejo, *J. Solid State Chem.*, 1976, **17**, 299–303.
13 Z. X. Chen, A. Derking, W. Koot and M. P. van Dijk, *J. Catal.*, 1996, **161**, 730–741.
14 S. F. Wang, F. Gu, M. K. Lü, C. F. Song, D. Xu, D. R. Yuan and S. W. Liu, *Chem. Phys. Lett.*, 2003, **373**, 223–227.
15 S. F. Wang, M. K. Lü, F. Gu, C. F. Song, D. Xu, D. R. Yuan, S. W. Liu, G. J. Zhou and Y. X. Qi, *Inorg. Chem. Commun.*, 2003, **6**, 185–188.
16 W. Wu, Y. W. Cai, J. F. Chen, S. L. Shen, A. Martin and L. X. Wen, *J. Mater. Sci.*, 2006, **41**, 5845–5850.
17 H. T. Kim, S. Nahm, J. D. Byun and Y. Kim, *J. Am. Ceram. Soc.*, 1999, **82**, 3476–3480.
18 J.-Z. Kong, A.-D. Li, H.-F. Zhai, H. Li, Q.-Y. Yan, J. Ma and D. Wu, *J. Hazard. Mater.*, 2009, **171**, 918–923.
19 F. H. Dulin and D. E. Rase, *J. Am. Ceram. Soc.*, 1960, **43**, 125–131.
20 S. F. Bartram and R. A. Slepetys, *J. Am. Ceram. Soc.*, 1961, **44**, 493–499.
21 M. R. Mohammadi and D. J. Fray, *J. Eur. Ceram. Soc.*, 2010, **30**, 947–961.
22 O. Yamaguchi, M. Morimi, H. Kawabata and K. Shimizu, *J. Am. Ceram. Soc.*, 1987, **70**, c97–c98.
23 Y. S. Chang, Y. H. Chang, I. G. Chen, G. J. Chen and Y. L. Chai, *J. Cryst. Growth*, 2002, **243**, 319–326.
24 X. H. Zeng, Y. Y. Liu, X. Y. Wang, W. C. Yin, L. Wang and H. X. Guo, *Mater. Chem. Phys.*, 2002, **77**, 209–214.
25 X. W. Wang, Z. Y. Zhang and S. X. Zhou, *Mater. Sci. Eng., B*, 2001, **86**, 29–33.
26 Z. Surowiak, M. F. Kupriyanov and D. Czekaj, *J. Eur. Ceram. Soc.*, 2001, **21**, 1377–1381.
27 H. Q. Fan and H. E. Kim, *Jpn. J. Appl. Phys.*, 2002, **41**, 6768–6772.
28 R. W. Schwartz, *Chem. Mater.*, 1997, **9**, 2325–2340.
29 J. Mrazek, L. Spanhel, G. Chadeyron and V. Matejec, *J. Phys. Chem. C*, 2010, **114**, 2843–2852.
30 D. Wang, J. Ye, T. Kako and T. Kimura, *J. Phys. Chem. B*, 2006, **110**, 15824–15830.
31 Y. F. Wang, K. H. Lee, H. Ohta and K. Koumoto, *Ceram. Int.*, 2008, **34**, 849–852.
32 B. G. Shabalin, *Mineral. Zh.*, 1982, **4**, 54–61.
33 C. H. Perry and D. B. Hall, *Phys. Rev. Lett.*, 1965, **15**, 700–702.
34 L. Hou, Y.-D. Hou, M.-K. Zhu, J. Tang, J.-B. Liu, H. wang and H. Yan, *Mater. Lett.*, 2005, **59**, 197–200.
35 U. Sulaeman, S. Yin and T. Sato, *Appl. Catal., B*, 2011, **105**, 206–210.
36 S. Kumar, T. Surendar, A. Baruah and V. Shanker, *J. Mater. Chem. A*, 2013, **1**, 5333–5340.
37 J. A. McLeord and A. Moewes, *Phys. Rev. B: Condens. Matter Mater. Phys.*, 2012, **86**, 195207.
38 K. V. Benthem, C. Elsasser and R. H. French, *J. Appl. Phys.*, 2001, **90**, 6156–6164.
39 F. M. F. De Groot, J. Faber, J. J. M. Michiels, M. T. Czyzyk, M. Abbate and J. C. Fuggle, *Phys. Rev. B: Condens. Matter Mater. Phys.*, 1993, **48**, 2074–2080.
40 S. Yin and T. Sato, *Ind. Eng. Chem. Res.*, 2000, **39**, 4526–4530.
41 H. Gerischer and A. Heller, *J. Phys. Chem.*, 1991, **95**, 5261–5267.